



Partial oxidation of surrogate Jet-A fuel over SiO₂ supported MoO₂

Shreya Shah^a, Oscar G. Marin-Flores^b, Karthik Chinnathambi^c, M. Grant Norton^{b,*}, Su Ha^{a,*}

^a Voiland School of Chemical Engineering and Bioengineering, Washington State University, Pullman, WA 99164, USA

^b School of Mechanical and Materials Engineering, Washington State University, Pullman, WA 99164, USA

^c Department of Materials Science and Engineering, Boise State University, Boise, ID 83725, USA

ARTICLE INFO

Article history:

Received 20 November 2015

Received in revised form 13 February 2016

Accepted 27 March 2016

Available online 7 April 2016

Keywords:

Partial oxidation

Jet-A fuel

SiO₂ support

MoO₂ nanoparticle and sintering

ABSTRACT

A SiO₂-supported MoO₂ nanoparticle catalyst was synthesized by a sol-gel method and tested as catalytic material for the partial oxidation of *n*-dodecane. MoO₂ nanoparticles supported on SiO₂ are <10 nm in size and show a resistance to sintering at 850 °C, which is a typical reforming temperature for *n*-dodecane. The formation of Mo–O–Si bonds at the interface between MoO₂ nanoparticles and SiO₂ support appear to be responsible for the enhanced stability to sintering displayed by the nanoparticles. As a result of this particle size stabilization, SiO₂ supported MoO₂ nanoparticles show an improved reforming activity in terms of syngas generation compared to micron-size commercial MoO₂. Thus, commercial MoO₂ exhibits a good initial activity at space velocities up to 15 h^{−1}, but showing only gas-phase reactions at larger values. Conversely, MoO₂ nanoparticles supported on SiO₂ show a high initial reforming activity (e.g., 69% H₂ yield, 82% CO yield and 100% carbon conversion) even at space velocities up to 30 h^{−1}. Supported MoO₂ nanoparticles also show good stability for the partial oxidation of *n*-dodecane at 850 °C without any sign of deactivation during the first 24 h on-stream.

© 2016 Elsevier B.V. All rights reserved.

1. Introduction

Comparisons of U.S. energy consumption and production at the end of 2013 showed an energy deficit of around 15 quadrillion Btu [1]. This energy deficit can be partially addressed in the future by development of more efficient approaches to energy conversion, e.g., improvement on conventional gas turbine and internal combustion engines [2]. These types of engines generate electricity via fuel combustion reactions, followed by converting the generated heat into mechanical energy and finally to electricity. Besides the thermodynamic limitations imposed by the Carnot cycle efficiency, the transformation of chemical energy into electrical energy in turbine engines leads to large energy losses due to the involvement of multiple conversion steps [3].

Fuel cells allow a more efficient conversion of the chemical energy of logistic fuels into electrical energy [3]. A recent study conducted by the Pacific Northwest National Laboratory (PNNL) has demonstrated that a fuel cell system can achieve an overall system efficiency >60%, when directly operated with liquid logistic fuels [4].

Amongst the different types of fuel cells, solid oxide fuel cells (SOFC) have garnered considerable interest, mainly due to their high operating temperature, which allows the required redox reactions to be catalyzed by inexpensive non-noble metals such as nickel. Furthermore, SOFC can operate with either H₂ or a mixture of H₂ and CO (syngas) as energy carrier. At the anode, the fuel reacts with oxygen ions transported from the cathode to generate electricity as the main product and water, or a mixture of water and carbon dioxide, as by-products. Pure H₂ can be obtained from syngas by treating it via water-gas shift reaction, followed by preferential CO oxidation and then separating H₂ and CO₂ [5]. This pure H₂ stream can be fed to polymer electrolyte membrane (PEM) fuel cells. Therefore, syngas is the main intermediate energy carrier and it has the potential to power multiple types of fuel cell.

Syngas can be produced by reforming various types of carbon sources, including conventional logistic fuels such as gasoline, diesel and jet fuels [6–10]. In future, reforming of biofuels such as biodiesel can be a source of syngas [11]. The advantage of using biofuels is that it can offer a net zero carbon emission for the entire energy cycle by capturing the emitted CO₂ from the fuel cell system via photosynthesis [12]. The utilization of these sustainable liquid fuels for fuel cells in automobile applications is particularly important because the current storage and distribution infrastructure of fossil-based transportation fuels is compatible with liquid biofuels

* Corresponding authors.

E-mail addresses: mg.norton@wsu.edu (M.G. Norton), suha@wsu.edu (S. Ha).

[13]. Thus, for automobile applications of fuel cells, we need on-board reformers that are compact and have the ability to efficiently convert liquid transportation fuels into syngas.

Three different reforming technologies can be considered for the production of syngas from liquid transportation fuels: steam reforming, partial oxidation, and autothermal reforming. Even though steam reforming is the most conventional approach to syngas generation, it is an endothermic process and, thus, requires external energy input. In addition, due to the requirement for additional space to store and distribute external water, steam reforming requires a larger overall system size with added complexity. Autothermal reforming combines both steam reforming and partial oxidation, and therefore it faces the same challenges as the steam reformers. On the other hand, reformers for catalytic partial oxidation (CPO) are compact, have faster start-up and quick response times, making them an ideal candidate for on-board syngas generation [14]. However, in order to directly process liquid transportation fuels, CPO reformers require a catalyst, which has the ability to reform long chain hydrocarbons, is coke resistant, sulfur tolerant, and is stable at high reforming temperatures.

MoO₂-based catalysts have shown reforming activity for complex and heavy liquid hydrocarbons such as isooctane, *n*-dodecane, gasoline and Jet-A fuel with both high coke resistance and sulfur tolerance [15–18]. Marin-Flores et al. discussed the activity of unsupported nanoparticle MoO₂ for the partial oxidation of *n*-dodecane [16]. The catalyst showed excellent coking resistance and reforming activity with 80% conversion and 85% H₂ yield at 850 °C, 1 atm, O₂/C=0.5 and weight hourly space velocity (WHSV) = 1.1 h⁻¹. However, at the high reforming temperature of 850 °C, MoO₂ is prone to sintering. In the literature two mechanisms are recognized for sintering [19]. In Oswald ripening atoms detach from smaller crystallites, migrate and attach to larger crystallites, resulting in crystal growth. The other mechanism involves migration of the entire crystallite followed by attachment and coalescence. Crystal growth can occur via either of these two mechanisms or as a culmination of both processes together. Although the sintering mechanism for MoO₂ nanoparticles is not exactly known, both mechanisms are temperature dependent. The Tamman temperature, T_{Tamman}, represents the minimum onset temperature for sintering [19]:

$$T_{\text{Tamman}}(\text{K}) = 0.5 T_{\text{Melting-point}}(\text{K}) \quad (1)$$

Since the melting temperature of MoO₂ is 1370 K, according to Eq. (1), MoO₂ nanoparticles begin sintering above 685 K (i.e., >410 °C). Since typical reforming temperatures of logistic fuels are >700 °C, unsupported MoO₂ nanoparticles would lose their active surface area quickly once the reaction starts. With low active surface areas, MoO₂-based reforming systems can only operate at low WHSVs, which lead to the low H₂ production rate.

Sintering can be prevented either by supporting the nanoparticles on a high surface area support or alloying the nanoparticles with additional elements [19]. For this study, we chose to support MoO₂ nanoparticles on a SiO₂ support. Silica was chosen as the support because it offers high surface area and it does not possess activity for fuel reforming [19–24]. Thus, it would not significantly alter the catalytic properties of the MoO₂ nanoparticles. The support can prevent sintering by either entrapping the nanoparticles within the silica network or by forming chemical bonds across the hetero-phase interface. Jung and Park synthesized silica-supported TiO₂ nanoparticles via the sol-gel method and investigated the effect of the support on particle sintering. According to their study, the formation Ti–O–Si bonds improve the sintering resistance of TiO₂ nanoparticles at high temperatures [25]. In the present study, we synthesized SiO₂ supported MoO₂ nanoparticles utilizing a similar sol-gel method and investigated the effect of the silica support on the sintering behavior of MoO₂ nanoparticles at high reforming

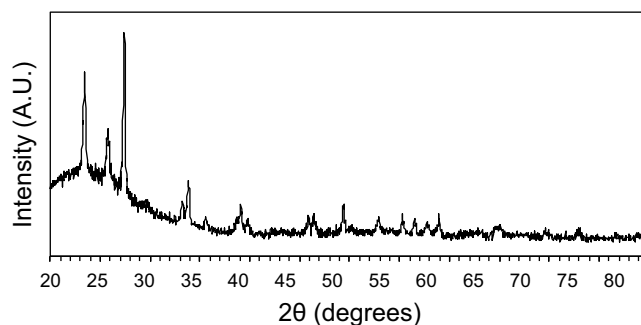


Fig. 1. XRD pattern of 10 mol% MoO₃–SiO₂.

temperatures. Finally, we tested the activity of the supported catalyst for the partial oxidation of surrogate Jet-A fuel (i.e., *n*-dodecane) at various WHSVs. The main objective of this study is to operate a MoO₂-based reforming unit at the highest possible WHSV and achieve a high H₂ production rate.

2. Experimental

2.1. Catalyst synthesis

The supported catalysts used in this study were synthesized using the sol-gel approach. All the chemicals and reagents were obtained from Alfa Aesar. Ammonium heptamolybdate tetrahydrate (AHM) is the molybdenum precursor and tetraethyl orthosilicate (TEOS) is used as a silicon precursor. Samples with a composition of 10 mol% MoO₃–SiO₂ were synthesized following the procedure described by Umbarkar et al. [26]. The resulting catalysts were reduced inside a quartz tube reactor using 10% H₂ in Ar at 450 °C for 3 h. Pure SiO₂ was synthesized by the sol-gel method described above, except the molybdenum precursor was replaced by 20% (by volume) ammonium hydroxide solution. Unsupported nanoparticle MoO₂ was synthesized by the autoclave method described in Marin-Flores et al. [16] and it was used for our temperature programmed reduction (TPR) experiments.

2.2. Characterization

The catalysts were characterized using various techniques. Siemens D-500 X-Ray powder diffractometer with a Cu Kα radiation was used for crystal structure analysis. The morphology of the powder samples was examined using both scanning electron microscopy (SEM; FEI Quanta 200F) and high-resolution transmission electron microscopy (TEM; JEOL JEM 2100HR operated at 200 kV). The samples for SEM were mounted on carbon tape and the SEM was operated at 30 kV and a spot size of 3. TEM samples were prepared by dispersing the powders in acetone and drop casting them on 3 mm carbon coated grids. A Chemisorb 2720 equipped with a thermal conductivity detector (TCD) was used for temperature programmed reduction (TPR). A quantity, 30 mg, of sample was taken in a U-shaped quartz tube and degassed under He at a flow rate of 20 ml/min and at a temperature of 400 °C for 30 min. Then the samples were cooled to 50 °C in He under the same flow rate. For TPR, the sample was heated in flowing 5% H₂/He from 50 °C to 1000 °C. BET surface area was measured by N₂ sorption experiments using a Micromeritics TriStar 3020 physisorption analyzer. Prior to measurements, the samples were degassed at 300 °C, under vacuum (<= 100 Torr), for 1 h. Diffuse reflectance infrared Fourier transformed spectroscopy (DRIFTS) measurements were performed using a Nicolet iS50 FTIR. The catalyst samples were mixed with KBr and the measurements were conducted by obtaining 128 scans at 4 cm⁻¹ resolution.

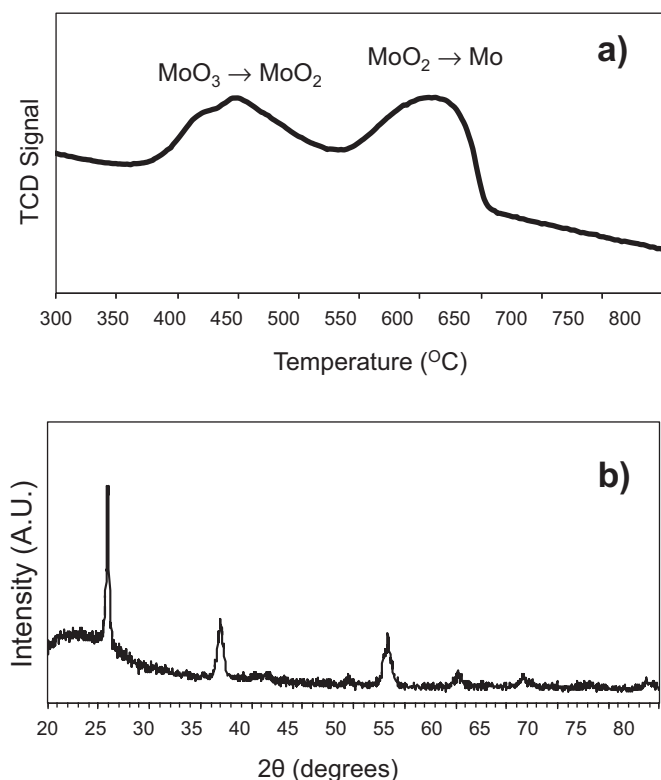


Fig. 2. (a) Temperature-programmed reduction (TPR) of 10 mol% MoO₃-SiO₂ in 5% H₂/He at 5 °C/min, and (b) diffractogram of 10 mol% MoO₃-SiO₂ after the reduction with a pure H₂ stream at 450 °C for 3 h.

2.3. Catalytic activity

The reforming activity of the catalysts was measured in a quartz tube reactor set-up as described previously by Marin-Flores et al. [16]. The flow rates of reactants were adjusted to obtain the desired O₂/C ratio. The gaseous products were analyzed using a gas chromatography (Molecular Sieve 5A Packed Column and HayeSep T Packed Column) with a TCD detector and the catalyst performance was evaluated in terms of H₂ yield, CO yield and carbon conversion, which are defined as shown below:

$$\text{H}_2 \text{ yield} = \frac{2 \times \text{moles of H}_2 \text{ produced}}{26 \times \text{moles of } n\text{-dodecane fed}} \times 100\%$$

$$\text{CO yield} = \frac{\text{moles of CO produced}}{12 \times \text{moles of } n\text{-dodecane fed}} \times 100\%$$

$$\text{Carbon Conversion} = \frac{\text{moles of (CO+CO}_2\text{+CH}_4\text{+2} \times \text{C}_2\text{H}_4\text{) produced}}{12 \times \text{moles of } n\text{-dodecane fed}} \times 100\%$$

The WHSV was calculated by dividing the weight of the feed stream (i.e., a mixture of *n*-dodecane and air) per unit time by the weight of MoO₂.

3. Results and discussion

3.1. Catalyst synthesis

Fig. 1 shows the X-ray diffraction pattern for a sample obtained after calcination at 500 °C. The diffractogram of the sample can be entirely indexed to orthorhombic MoO₃, which is believed to form as a result of the complete conversion of the isopolymolybdate species to a pure Mo (VI) oxide. Based on the Scherrer equation, the average crystallite size is estimated to be 24 nm with a stan-

Table 1

Physical properties of pure SiO₂, fresh MoO₂/SiO₂ and annealed MoO₂/SiO₂ samples.

	BET surface area (m ² /g)	Pore volume (cm ³ /g)
Pure SiO ₂	241	1.33
Fresh MoO ₂ /SiO ₂	301	1.08
Annealed MoO ₂ /SiO ₂	18	0.04

dard deviation of 7 nm. The broad peak at 2θ below 35° represents the amorphous SiO₂ support.

In order to obtain 10 mol% MoO₂-SiO₂, the calcined material needs to be reduced. In the literature, bulk MoO₃ has been reduced between 400 and 600 °C to obtain the MoO₂ phase [27–29]. However, due to the presence of many suboxides (e.g., Mo₁₈O₅₈, Mo₈O₂₃, MoO) and the tendency of nanoparticles to have lower reduction temperatures than their parent bulk materials, temperature programmed reduction (TPR) experiments were performed to determine the suitable temperature for the reduction of MoO₃ to MoO₂ for our calcined samples [30]. The profile obtained in Fig. 2a exhibits two major peaks: one at 450 °C and another one centered around 620 °C. Based on previous reports [27], the low temperature peak in the TPR profile can be attributed to the reduction of MoO₃ to MoO₂, while the higher temperature peak is assigned to the reduction of MoO₂ to Mo metal. The peak at 450 °C has a noticeable shoulder at 420 °C. Generally, the reduction MoO₃ to MoO₂ is considered a two-step reduction via an intermediate [27]. The shoulder at 420 °C can be attributed to the reduction of MoO₃ to the intermediate and then to MoO₂ at 450 °C. To prevent excessive reduction with the subsequent formation of metallic Mo, the temperature in the reduction step to produce silica-supported MoO₂ was set to 450 °C. Fig. 2b shows the diffraction pattern of the sample obtained from the calcination step after the reduction under pure H₂ at 450 °C for 3 h. The diffractogram shows peaks that can be indexed exclusively to the monoclinic MoO₂ phase along with the characteristic broad peak for silica at 2θ < 35°. The average crystallite size of MoO₂ calculated using the Scherrer equation is 15 nm with a standard deviation of 7 nm.

3.2. Resistance to sintering at 850 °C

The effectiveness of silica as a support is determined by its ability to prevent sintering. For the sintering test, the synthesized catalysts were annealed under N₂ for 0.5 h at 850 °C. XRD, TEM and BET surface area measurements were performed for the annealed catalysts and compared with as-synthesized catalysts (Table 1). Compared to a pure SiO₂ support, the surface area increases after the addition of MoO₂ over the SiO₂ support from 241 m²/g to 301 m²/g. However, the pore volume shows a decrease from 1.33 cm³/g to 1.08 cm³/g. The increase in the surface area can be attributed to the addition of MoO₂ nanoparticles, while the decrease in the pore volume can be due to the presence of MoO₂ crystallites occupying the intra-particle pores. The surface area decreases drastically from 301 m²/g for as-synthesized catalysts to 18 m²/g after annealing. The pore volume shows a similar trend and decreases to 0.04 cm³/g. The decrease in the surface area and pore volume can be explained due to the densification of the SiO₂ support (as seen later in the TEM images). Even though the silica support shows densification at high temperatures resulting in a low surface area, the nanoparticle MoO₂ does not show sintering and maintains its nanoparticle size at 850 °C (as evident from both TEM and XRD crystallite size measurements) Table 2.

Fig. 3 shows representative TEM images of the samples used in this work. As shown in Fig. 3a, as synthesized SiO₂ particles have an equiaxed morphology with a size around 20 nm. In Fig. 3b the initial MoO₂ nanoparticles dispersed on the silica before the annealing are clearly visible and are ≤10 nm, which is in good agreement

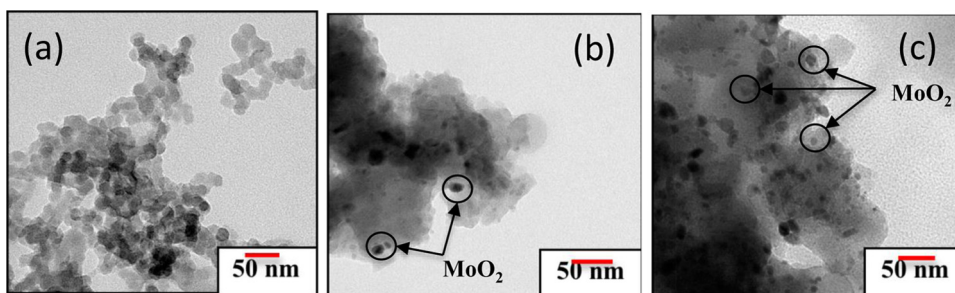


Fig. 3. TEM images of (a) SiO₂, (b) MoO₂–SiO₂ as synthesized, and (c) MoO₂–SiO₂ after annealing for 2 h at 850 °C in nitrogen.

Table 2

Vibration mode for 10 mol% MoO₂–SiO₂ DRIFTS.

Vibration Mode (cm ⁻¹)	Bond
802	Asymmetric $\nu(\text{Si-O-Si})$
956	$\nu(\text{Si-O-H})$
965	$\nu(\text{Si-O-Mo})$
1095	Symmetric $\nu(\text{Si-O-Si})$

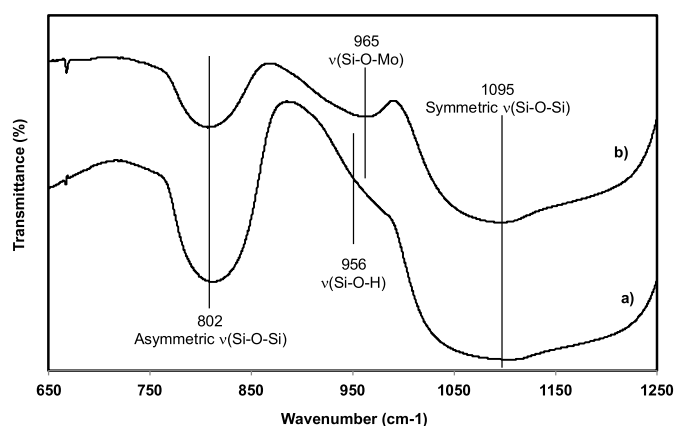


Fig. 4. DRIFTS of (a) fresh SiO₂ and (b) as-synthesized 10 mol% MoO₂–SiO₂.

with the estimates from the XRD data. Comparison of Fig. 3a and b shows that the SiO₂ particles have sintered during the reduction process. The post-annealing sample at 850 °C shown in Fig. 3c suggests that the annealing process was not able to produce significant changes in the morphology of the MoO₂ nanoparticles; the size after annealing is ≤ 10 nm.

In order to understand the role of the silica support in preventing sintering of nanoparticle MoO₂ at high temperatures, DRIFTS and activation energy measurements (via TPR) were performed. Fig. 4 shows the transmittance spectra for SiO₂ and as-synthesized 10 mol% MoO₂–SiO₂. The SiO₂ spectrum (Fig. 4a) shows three characteristic peaks at 802 cm⁻¹, 956 cm⁻¹ and 1095 cm⁻¹ corresponding to symmetric $\nu(\text{Si-O-Si})$, $\nu(\text{Si-O-H})$ and asymmetric $\nu(\text{Si-O-Si})$, respectively [31]. For 10 mol% MoO₂–SiO₂ samples, the high intensity peaks of SiO₂ suppress peaks that are characteristic for MoO₂ nanoparticles (e.g., 739 cm⁻¹ (Mo–O), 696 cm⁻¹ (O–Mo–O), 960 cm⁻¹ (Mo=O) and 860 cm⁻¹ (Mo–O–Mo)). Nevertheless, the as-synthesized 10 mol% MoO₂–SiO₂ sample shows peaks for SiO₂ (802 cm⁻¹ for symmetric $\nu(\text{Si-O-Si})$ and 1095 for asymmetric $\nu(\text{Si-O-Si})$) and a peak shift for $\nu(\text{Si-O-H})$ towards higher wavenumber to 965 cm⁻¹. This shift can be explained by replacement of H with Mo to form Si–O–Mo [32]. A similar shift has been reported in the literature for silica supported TiO₂, where the formation Ti–O–Si bonds improves the sintering resistance [25]. Based on our DRIFTS data, we can speculate that the formation

of Si–O–Mo bonds at the MoO₂–SiO₂ interface could anchor the MoO₂ nanoparticles and, therefore, prevent sintering.

The energy of activation, E_a , for the reduction process was measured for supported and unsupported nanoparticle MoO₂ using the Kissinger equation [33], in order to further investigate the effect of the MoO₂–SiO₂ interaction observed in DRIFTS:

$$\ln \left[\frac{\psi}{T_{\max}^2} \right] = \frac{-E_a}{RT_{\max}} + \ln \left[\frac{AR}{E_a} \right] \quad (2)$$

In the Kissinger equation (Eq. (2)) ψ is the heating rate, T_{\max} is the peak temperature, A is a pre-exponential factor, and R is the gas constant. Samples of both catalysts were reduced at different ψ and E_a was calculated using the slope of the straight line resulting from the plot of $\ln [\psi/T_{\max}^2]$ versus $1/T_{\max}$. The TPR profiles of unsupported and silica-supported MoO₂ are shown in Fig. 5a and b, respectively. Fig. 5c displays the data appropriately arranged to determine E_a for the reduction of both samples with H₂. As seen, for the unsupported MoO₂ sample, the value of E_a was found to be 99 ± 3 kJ/mol whereas for the silica supported MoO₂ sample the value obtained was 104 ± 6 kJ/mol. Thus, the reducibility of MoO₂ with and without the support appears to be very similar, which suggests that the interaction is present only at the interface and it does not affect the bulk property of the catalysts.

To further investigate the effect of the interfacial interaction, the dispersion of MoO₂ over SiO₂ was calculated for the annealed sample using Eqn. 3. The assumptions are that the crystallites have a circular cross section and the surface density is 14.69 Mo atoms/nm² for MoO₂:

$$\% \text{Dispersion} = \frac{\text{Mo atoms on crystallite surface}}{\text{Total Mo atoms in crystallite}} \quad (3)$$

Based on this calculation, the dispersion of MoO₂ over SiO₂ for as-synthesized 10 mol% MoO₂–SiO₂ sample was 21%. This low dispersion value can further explain why the interaction at the interface does not affect the bulk catalytic properties. Thus, we propose that the prevention of sintering of the nanoparticles is mainly caused by the interfacial interaction between MoO₂ and SiO₂. The interaction is strong enough to prevent sintering and grain growth of the MoO₂ nanoparticles, but it does not affect the bulk properties due to the low dispersion.

3.3. Catalyst activity for partial oxidation of *n*-dodecane

Activity tests for the partial oxidation of *n*-dodecane were conducted for both unsupported MoO₂ (commercial MoO₂) and supported nanoparticle MoO₂ on SiO₂. The reaction conditions were chosen based on thermodynamic and experimental analysis performed by Marin-Flores et al. for the partial oxidation of *n*-dodecane over unsupported MoO₂ nanoparticles [18]. According to their experimental results and thermodynamic calculations, the highest stability for the MoO₂ phase can be achieved at 850 °C and 1 atm using O₂/C ratios between 0.5 and 1.0. However, if the O₂/C

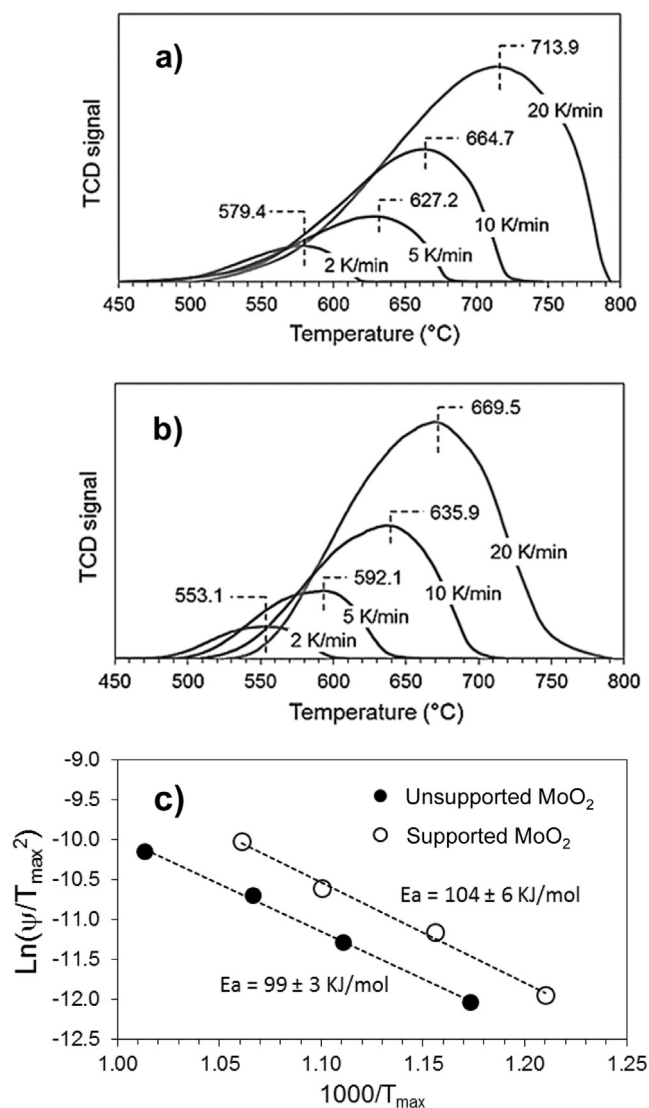


Fig. 5. (a) TPR of as-synthesized 10 mol% MoO₂-SiO₂ with a change in the ramping rate, (b) TPR of unsupported MoO₂ with a change in the ramping rate and (c) E_a energy calculation for supported and unsupported MoO₂ based on their TPR data.

ratio is too high and closer to 1.0, the production rate of syngas is low due to the formation of large concentrations of H₂O and CO₂. On the other hand, if the O₂/C ratio is too low and closer to 0.5, the tendency for the coke formation significantly increases. Therefore, an O₂/C ratio of 0.7 was used for the present study in order to stabilize the MoO₂ phase without becoming detrimental for the syngas production.

Fig. 6a shows % H₂ yield, % CO yield and % carbon conversion for the partial oxidation of *n*-dodecane over commercial MoO₂ at different WHSVs after operating the catalyst for 4.5 h. Fig. 6a also includes the blank run for comparison purposes. In the absence of the catalyst (blank run), 21% H₂ yield, 75% CO yield and 95% carbon conversion were measured. According to the thermodynamic calculations performed by Marin-Flores et al., the equilibrium H₂ and CO yields are between 80 and 85% under the given reforming conditions [18]. Thus, the H₂ yield for the blank run is much lower compared to the equilibrium H₂ yield, while the CO yield is just slightly lower than the equilibrium CO yield. In addition to H₂ and CO, the blank run also produced 3% CH₄ yield, 15% C₂H₄ yield and 19% CO₂ (not shown in Fig. 6a). The main reaction taking place in the reformer at 850 °C for the blank run is thermal cracking,

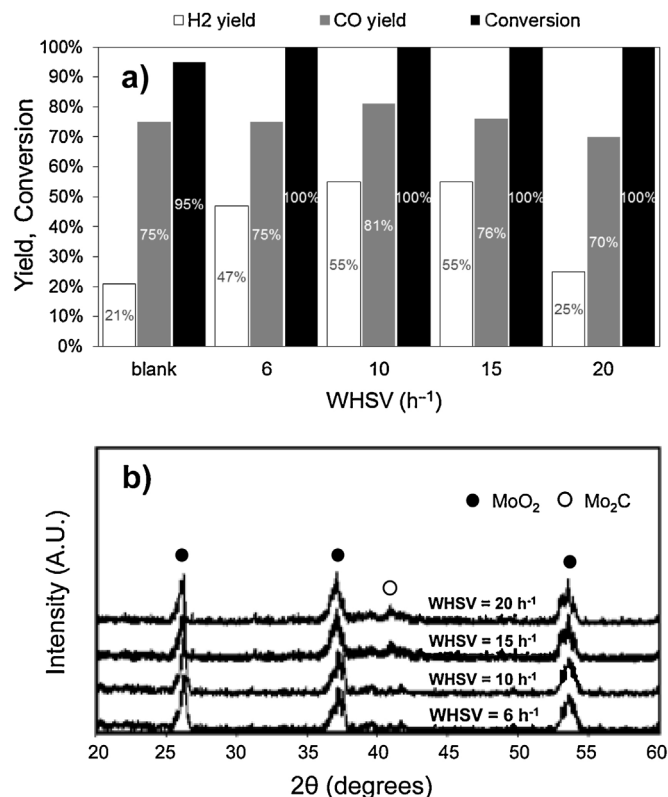


Fig. 6. (a) Catalytic performance of the commercial MoO₂ for the partial oxidation of *n*-dodecane at various WHSVs (1 atm, 850 °C and O₂/C = 0.7), and (b) XRD patterns of samples at the end of the activity tests after time-on-stream of 4.5 h shown in (a).

which leads to the formation of C₁ and C₂ products. Even though the carbon conversion is as high as 95%, its selectivity towards H₂ gas generation is too low for fuel cell applications, as deduced from the low hydrogen yield of 21%.

According to Fig. 6a, commercial MoO₂ provides 100% carbon conversion for WHSVs ranging between 6 and 20 h⁻¹. The conversion increases by 5% compared to that of the blank run irrespective of the WHSV. When compared to the blank run, the H₂ yield for commercial MoO₂ at WHSV of 15 h⁻¹ significantly increases from 21% to 55%. However, there is almost no change in the CO yield (75%–76%), while the CO₂ yield only increases by 6%. This increase in H₂ yield for commercial MoO₂ can be partially explained by the enhanced reforming activities toward CH₄ and C₂H₄ compounds over the MoO₂ surface as no CH₄ yield is observed and C₂H₄ yield drops from 15% to 12% in the product stream when the commercial MoO₂ catalyst was used at a WHSV of 15 h⁻¹. Moreover, the fuel mixture, in the absence of catalyst, would continuously decompose in the gas phase as it flows through the reactor. The blank test suggests that most of the fuel is fully decomposed in the gas phase to form either CO or CO₂ with low H₂ selectivity at the outlet of the reactor. However, in the presence of the catalyst, the partially decomposed fuel molecules or carbon fragments react over the catalyst bed before they have a chance to fully decompose to either CO or CO₂ in the gas phase. Compared to the blank test, our activity test results indicate that this catalytic partial oxidation reaction favors the production of H₂ (probably by decreasing H₂O selectivity), leading to a higher H₂ yield. As the WHSV increases from 15 to 20 h⁻¹, the H₂ yield decreases and eventually becomes comparable to the blank run as shown in Fig. 6a. The loss of selectivity towards H₂ at high WHSV of 20 h⁻¹ for commercial MoO₂ can be attributed to its large particle size (50–200 nm) and low surface area (4 m²/g) [16]. With an increase in WHSV, the amount of fuel that flows over

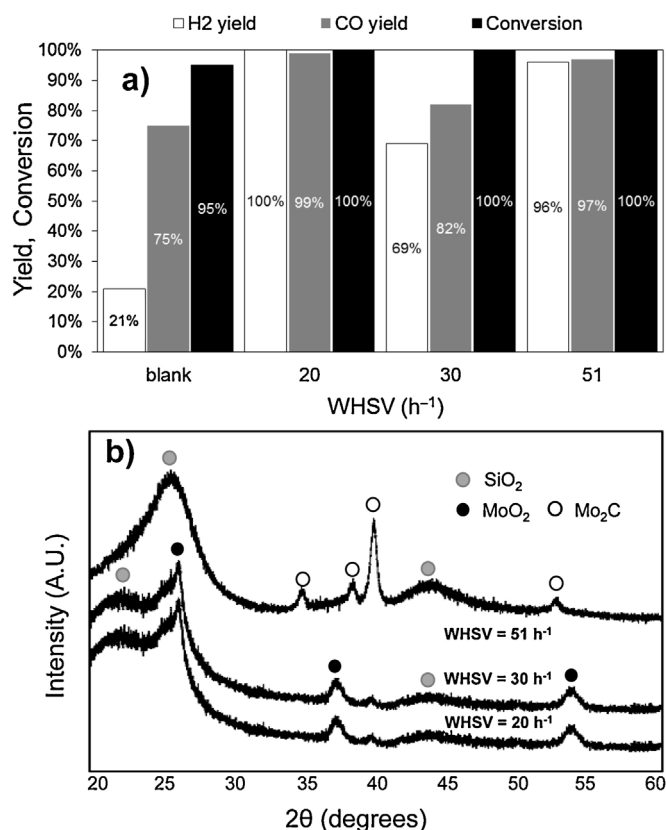


Fig. 7. (a) Catalytic performance of the silica-supported MoO₂ for the partial oxidation of *n*-dodecane at various WHSVs (1 atm, 850 °C and O₂/C = 0.7), and (b) XRD patterns of samples at the end of the activity tests shown in (a).

the catalyst bed per unit time increases. Due to the low surface area of commercial MoO₂, it does not offer enough active sites to catalytically reform all the fuel molecules at high WHSV values. Therefore, a large portion of the fuel molecules undergo gas phase decomposition reaction, rather than catalytic partial oxidation and thus produce a lower % H₂ yield. The diffractograms from the spent samples shown in Fig. 6b indicate that the MoO₂ phase is the predominant crystalline phase with a small amount of Mo₂C present in all cases.

For supported MoO₂, the activity tests were performed for the partial oxidation of *n*-dodecane at the same reaction conditions used for the unsupported MoO₂. The results as a function of WHSV are shown in Fig. 7a. At a WHSV of 20 h⁻¹, the supported MoO₂ shows average values of ~100% for % H₂ yield, % CO yield and % carbon conversion. Using MoO₂ nanoparticles supported on SiO₂ not only produces the complete carbon conversion, it also shows an improvement in the selectivity towards syngas production (i.e., an increase in % H₂ and % CO yields). The H₂ yield and CO yield are higher than their respective equilibrium values by 15–20%. This discrepancy indicates that there are many reactions (both gas phase and heterogeneous catalytic reactions) occurring over the catalyst bed of the reactor in a very complex way, which were not all accounted for by the previous thermodynamic studies [18].

Furthermore, no CO₂ yield was observed over the supported nanoparticle MoO₂ at a WHSV of 20 h⁻¹ (data not shown), whereas commercial MoO₂ shows a performance similar to the blank run with 20% CO₂ yield. As explained earlier, in the case of commercial MoO₂, the performance is similar to the blank run at high space velocities due to the low surface area, which enhances the undesired gas phase reactions. In the case of the supported MoO₂, the high surface area allows a large volume of fuel molecules to be pro-

cessed per unit time via surface partial oxidation, thus reducing the undesired gas phase reactions. Additionally, the nanoparticle size effect can also contribute to the enhanced catalytic reforming activity of the supported MoO₂. This particle size effect is a well-known phenomenon previously reported in the literature [34–36]: changing the particle size of the catalyst changes the selectivity towards desired products. Consequently, % H₂ and % CO yields of supported MoO₂ are much higher than those of commercial MoO₂ at high WHSV of 20 h⁻¹.

Marin-Flores et al. also showed similar results for unsupported MoO₂ nanoparticles for the partial oxidation of *n*-dodecane under reforming conditions similar to our present study except at WHSV ≤ 10 h⁻¹ [16]. Because unsupported MoO₂ nanoparticles can easily sinter at reforming temperatures, the active surface area would significantly decrease at the early stages of the reaction, producing a reforming activity similar to that of a blank run at high WHSVs. However, supported MoO₂ nanoparticles synthesized in our present study maintain their nanoparticle size and high surface area due to the interaction between the nanoparticles and the silica support, thus providing much increased active surface area even at high reforming temperatures.

As the WHSV is increased to 30 h⁻¹, the average conversion remains at 100% while the average yields of H₂ and CO drop to 82% and 69%, respectively. A further increase in WHSV to 51 h⁻¹ leads to an increase in average yields of both H₂ and CO, which reached values of 96% and 97%, respectively. This increase in syngas generation can be attributed to the phase change of MoO₂ into Mo₂C, as seen in the diffractograms of Fig. 7b. The MoO₂ is the stable phase up to WHSV of 30 h⁻¹ and it transforms to Mo₂C at a WHSV of 51 h⁻¹. The phase change at the high WHSV of 51 h⁻¹ is consistent with the thermodynamic study done by Marin-Flores et al. [18]. For the initial reforming performance, it seems that the supported Mo₂C nanoparticles are more active than that of supported MoO₂ nanoparticles toward the partial oxidation of *n*-dodecane. However, the phase change at high WHSVs is detrimental to the long-term performance as MoO₂ possesses the higher coking resistance than Mo₂C at high WHSVs. This is due to the high oxygen mobility of MoO₂, where lattice oxygen is more active than gas phase oxygen for reacting with the active carbon formed on the catalyst surface. Therefore, in the case of MoO₂, the lattice oxygen is readily available for scavenging any deposited carbon, whereas in the case of Mo₂C the carbon deposits slowly build upon the surface, leading to eventual deactivation.

In order to elucidate the above phenomena, 24 h activity tests were performed at WHSVs of 30 and 51 h⁻¹ for the supported MoO₂. Fig. 8a shows the catalyst performance at WHSV of 30 h⁻¹ for the supported MoO₂ sample. As seen, the catalyst exhibits a stable performance without any signs of deactivation over a period of 24 h, with the conversion of 100% and average H₂ and CO yields of 63% and 75%, respectively. The diffractogram of the sample at the end of the test (data not shown) indicates the presence of only the MoO₂ phase.

However, in case of a WHSV of 51 h⁻¹ for the supported MoO₂, the catalyst shows higher H₂ and CO yields with 100% carbon conversion for the first 5 h on stream (like that shown in the initial performance data in Fig. 7a) and then it slowly deactivates over the next 21 h on stream. This decrease in the performance over 21 h is attributed to excessive coke formation, which became evident as it was easily observed on the reactor walls. The XRD pattern of the spent sample (data not shown) indicated the presence of only Mo₂C.

Therefore, according to our 24-h activity test data, the catalyst shows both good initial activity and good stability at a WHSV of 30 h⁻¹, where it maintains the MoO₂ phase. However, if the WHSV increases to 51 h⁻¹, the supported MoO₂ nanoparticles are first transformed into Mo₂C followed by the gradual decreases in the

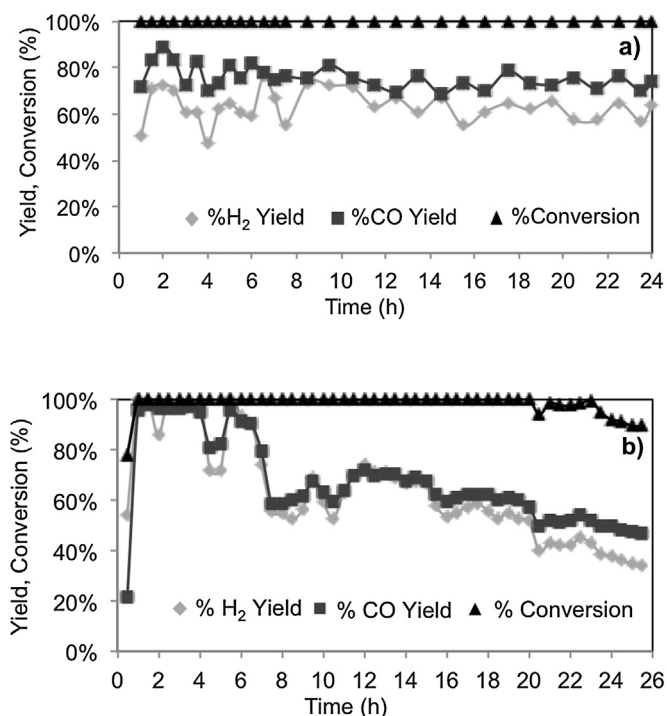


Fig. 8. Partial oxidation of *n*-dodecane over 10 mol% MoO₂–SiO₂ at 850 °C, 1 atm, O₂/C = 0.7 and two different WHSVs: (a) WHSV = 30 h^{−1} and (b) WHSV = 51 h^{−1}.

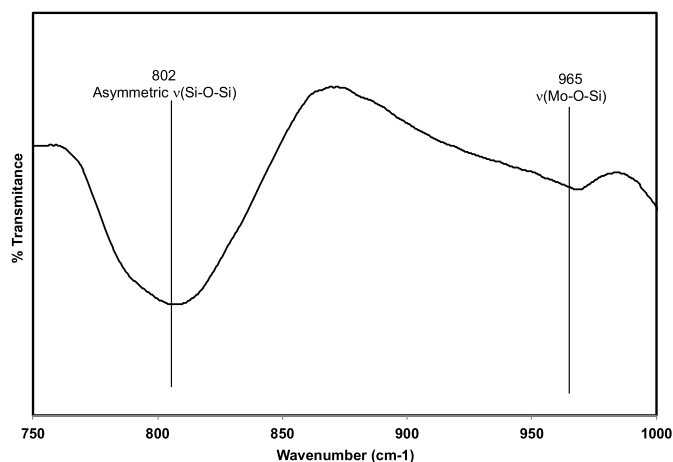


Fig. 9. DRIFTS of spent 10 mol% MoO₂–SiO₂ following the partial oxidation reaction of *n*-dodecane at 850 °C, 1 atm, O₂/C = 0.7 and WHSV = 30 h^{−1}.

performance (e.g., decrease of H₂ yield, CO yield and carbon conversion).

DRIFTS were obtained for the spent catalysts at WHSV of 30 h^{−1} in order to determine if the interaction between MoO₂ and SiO₂ was still present. As seen in Fig. 9, the spent catalysts also show the peak that is characteristic of the Mo–O–Si bond at 965 cm^{−1}. Thus, the catalysts maintain the interphase interaction between SiO₂ and MoO₂ during the reforming test, which is essential for maintaining nanoparticle MoO₂ and producing the high syngas generation rate over the 24 h period.

4. Conclusions

High surface area silica supported MoO₂ catalysts were synthesized by the sol-gel method. The surface area eventually drops to 18 m²/g after annealing at 850 °C. The reduction in surface area

is solely due to the sintering of silica and not due to sintering of the MoO₂ nanoparticles. As observed in TEM images, the MoO₂ crystallite size ranges from 2 to 10 nm. DRIFTS for the synthesized catalysts shows the presence of Mo–O–Si bonds, which helps in anchoring the MoO₂ nanoparticles to the silica surface and thus preventing sintering at high temperatures. The presence of an interaction between silica and MoO₂ at the interface does not affect the bulk property of the catalyst, as the activation energy for MoO₂ reduction is almost the same for both supported and unsupported catalysts. The low dispersion of the nanoparticles over the silica support might also play a contributing role to maintaining the bulk catalytic activity.

The supported MoO₂ nanoparticles show good catalytic activity and high selectivity towards syngas generation at high WHSVs with near 100% conversion, H₂ yield and CO yield at WHSV of 20 h^{−1}. The increase in selectivity towards syngas generation for supported MoO₂ nanoparticle is due to the maintenance of high surface areas at the reforming temperatures.

Silica supported MoO₂ nanoparticles show good initial catalytic activity at WHSVs up to 30 h^{−1}. At a WHSV of 51 h^{−1}, the MoO₂ transforms into Mo₂C. This phase change leads to an initial increase in syngas generation; however, deactivation due to severe coking occurs over a period of 21 h. The activity test for silica supported MoO₂ catalysts at a WHSV of 30 h^{−1} shows the good reforming performance over 24-h experiments with 100% conversion, 63% H₂ yield and 76% CO yield. The diffractogram of the spent catalyst obtained at a WHSV of 30 h^{−1} shows solely the MoO₂ phase. Therefore, in order to maintain a good catalytic activity over a long-term operation, the catalyst needs to be operated under conditions that favor the high stability of the MoO₂ phase.

Acknowledgement

This work was financially supported by the Office of Naval Research (Grant No. N00014-15-1-2416).

References

- [1] M. Joyce, R. Repice, Domestic production satisfies 84% of total U.S energy demand in 2013, E.I.A., monthly energy review, (2014) Retrieved from <http://www.eia.gov/todayinenergy/detail.cfm?id=16511>.
- [2] P. Biloen, W.M.H. Sachtler, Mechanism of hydrocarbon synthesis over Fischer–Tropsch catalysts, *Adv. Catal.* 30 (1981) 165–215.
- [3] A. Kirubakaran, S. Jain, R.K. Nema, A review on fuel cell technologies and power electronic interface, *Renew. Sustain. Energy Rev.* 13 (2009) 2430–2440.
- [4] G.G. Park, S.D. Yim, Y.G. Yoon, W.Y. Lee, C.S. Kim, D.J. Seo, K. Eguchi, Hydrogen production with integrated microchannel fuel processor for portable fuel cell systems, *J. Power Sources* 145 (2005) 702–706.
- [5] P. Gupta, L.G.V. Vargas, L.S. Fan, Syngas redox (SGR) process to produce hydrogen from coal derived syngas, *Energy Fuels* 21 (5) (2007) 2900–2908.
- [6] B.C. Michael, D.N. Nare, L.D. Schmidt, Catalytic partial oxidation of ethane to ethylene and syngas over Rh and Pt coated monoliths: spatial profiles of temperature and composition, *Chem. Eng. Sci.* 65 (2010) 3893–3902.
- [7] L. Wang, K. Murata, M. Inaba, A novel highly active catalyst system for CO₂ reforming of methane and higher hydrocarbons, *Catal. Commun.* 4 (2003) 147–151.
- [8] R.K. Kaila, A. Gutierrez, S.T. Korhonen, A.O.I. Krause, Autothermal reforming of *n*-dodecane, toluene, and their mixture on mono- and bimetallic noble metal zirconia catalysts, *Catal. Lett.* 115 (1–2) (2007) 70–78.
- [9] J.M. Mayne, A.R. Tadd, K.A. Dahlberg, J.W. Schwank, Influence of thiophene on the isooctane reforming activity of Ni based catalysts, *J. Catal.* 271 (1) (2010) 140–152.
- [10] M.C. Alvarez-Galvan, R.M. Navarro, F. Rosa, Y. Briceño, M.A. Rida, J.L.G. Fierro, Hydrogen production for fuel cell by oxidative reforming of diesel surrogate: influence of ceria and/or lanthana over the activity of Pt/Al₂O₃ catalysts, *Fuel* 87 (12) (2008) 2502–2511.
- [11] S. Shah, O. Marin-flores, M.G. Norton, S. Ha, Mo₂C supported NiMo alloys for synthesis gas production via partial oxidation of surrogate biodiesel, *J. Power Sources* 294 (2015) 530–536.
- [12] V. Klouz, V. Fierro, P. Denton, H. Katz, J.P. Lisse, S. Bouvot-Mauduit, C. Mirodatos, Ethanol reforming for hydrogen production in a hybrid electric vehicle: process optimization, *J. Power Sources* 105 (1) (2002) 26–34.

- [13] J.C. Amphlett, R.F. Mann, B.A. Peppley, P.R. Roberge, A. Rodrigues, J.P. Salvador, Simulation of a 250 kW diesel fuel processor/PEM fuel cell system, *J. Power Sources* 71 (1–2) (1998) 179–184.
- [14] D.A. Hickman, L.D. Schmidt, Production of syngas by direct catalytic oxidation of methane, *Science* 259 (1993) 343–346.
- [15] O.G. Marin-Flores, S. Ha, Activity and stability studies of MoO_2 catalyst for the partial oxidation of gasoline, *Appl. Catal. A* 352 (2009) 124–132.
- [16] O.G. Marin-Flores, T. Turba, C. Ellefson, K. Wang, J. Breit, J. Ahn, M.G. Norton, S. Ha, Nanoparticle molybdenum dioxide: a highly active catalyst for partial oxidation of aviation fuels, *Appl. Catal. B* 98 (2010) 186–192.
- [17] C.M. Cuba-Torres, O. Marin-Flores, C.D. Owen, Z. Wang, M. Garcia-Perez, M.G. Norton, S. Ha, Catalytic partial oxidation of a biodiesel surrogate over molybdenum dioxide, *Fuel* 146 (2015) 132–137.
- [18] O. Marin-Flores, T. Turba, J. Breit, M.G. Norton, S. Ha, Thermodynamic and experimental study of the partial oxidation of a Jet A fuel surrogate over molybdenum dioxide, *Appl. Catal. A* 381 (1–2) (2010) 18–25.
- [19] A. Cao, R. Lu, G. Vesper, Stabilizing metal nanoparticles for heterogeneous catalysis, *Phys. Chem. Chem. Phys.* 12 (2010) 13499–13510.
- [20] W. Li, M.O. Coppens, Synthesis and characterization of stable hollow Ti-silica microspheres with a mesoporous Shell, *Chem. Mater.* 17 (9) (2005) 2241–2246.
- [21] X. Fu, L.A. Clark, Q. Yang, M.A. Anderson, Enhanced photocatalytic performance of Titania-based binary metal oxides: $\text{TiO}_2/\text{SiO}_2$ and $\text{TiO}_2/\text{ZrO}_2$, *Environ. Sci. Technol.* 30 (1996) 647–653.
- [22] S.B. Umbarkar, A.V. Biradar, S.M. Mathew, S.B. Shelke, K.M. Malshe, P.T. Patil, S.P. Dagde, S.P. Niphadkar, M.K. Dongare, Vapor phase nitration of benzene using mesoporous $\text{MoO}_3/\text{SiO}_2$ solid acid catalyst, *Green Chem.* 8 (2006) 488–493.
- [23] M.T. Bore, H.N. Pham, E.E. Switzer, T.L. Ward, A. Fukuoka, A.K. Datye, The role of pore size and structure on the thermal stability of gold nanoparticles within mesoporous silica, *J. Phys. Chem. B* 109 (7) (2005) 2873–2880.
- [24] S.H. Joo, J.Y. Park, C.K. Tsung, Y. Yamada, P. Yang, G.A. Somorjai, Thermally stable Pt/mesoporous silica core-shell nanocatalysts for high-temperature reactions, *Nature Mater.* 8 (2009) 126–131.
- [25] K.Y. Jung, S.B. Park, Enhanced photoactivity of silica-embedded titania particles prepared by sol–gel process for the decomposition of trichloroethylene, *Appl. Catal. B: Environ.* 25 (2000) 249–256.
- [26] S.B. Umbarkar, A.V. Biradar, S.M. Mathew, S.B. Shelke, K.M. Malshe, P.T. Patil, S.P. Dagde, S.P. Niphadkar, M.K. Dongare, Vapor phase nitration of benzene using mesoporous $\text{MoO}_3/\text{SiO}_2$ solid acid catalyst, *Green Chem.* 8 (2006) 488–493.
- [27] P. Arnoldy, J.C.M. de Jonge, J.A. Moulijn, Temperature-programmed reduction of MoO_3 and MoO_2 , *J. Phys. Chem.* 89 (21) (1985) 4517–4526.
- [28] T. Ressler, R.E. Jentoft, J. Wienold, M.M. Gunter, O. Timpe, In situ XAS and XRD studies on the formation of Mo suboxides during reduction of MoO_3 , *J. Phys. Chem. B* 104 (2000) 6360–6370.
- [29] T. Ressler, J. Wienold, R.E. Jentoft, Formation of bronzes during temperature-programmed reduction of MoO_3 with hydrogen—an in situ XRD and XAFS study, *Solid State Ion.* 141–142 (2001) 243–252.
- [30] J.G. Lee, H. Mori, H. Yasuda, Alloy phase formation in nanometer-sized particles in the In–Sn system, *Phys. Rev. B* 65 (132106) (2002) 1–4.
- [31] M. Crisan, A. Jitianu, M. Zaharescu, F. Mizukami, S. Niwa, Sol–gel mono- and poly-component nanosized powders in the $\text{Al}_2\text{O}_3\text{--TiO}_2\text{--SiO}_2\text{--MgO}$ system, *J. Dispers. Sci. Technol.* 24 (1) (2003) 129–144.
- [32] M. Selvaraj, B.H. Kim, T.G. Lee, FTIR studies on selected mesoporous metallosilicate molecular sieves, *Chem. Lett.* 34 (9) (2005) 1290–1291.
- [33] A. Fraczyk, The activation energy of primary crystallization of Fe95Si5 metallic glass, *Tech. Sci.* 14 (1) (2011) 93–100.
- [34] G.L. Bezemer, J.H. Bitter, H.P.C.E. Kuipers, H. Oosterbeek, J.E. Holeyijn, X. Xu, F. Kapteijn, A.J.V. Dillen, K.P.D. Jong, Cobalt particle size effects in the Fischer–Tropsch reaction studied with carbon nanofiber supported catalysts, *J. Am. Chem. Soc.* 128 (12) (2008) 3956–3964.
- [35] H.M. Torres Galvis, J.H. Bitter, T. Davidian, M. Ruitenbeek, A.I. Dugulan, K.P.D. Jong, Iron particle size effects for direct production of lower olefins from synthesis gas, *J. Am. Chem. Soc.* 134 (2012) 16207–16215.
- [36] J. Kang, S. Zhang, Q. Zhang, Y. Wang, Ruthenium nanoparticles supported on carbon nanotubes as efficient catalysts for selective conversion of synthesis gas to diesel fuel, *Angew. Chem. Int. Ed.* 121 (2009) 2603–2606.